

Anisotropic self-assemblies of magnetic nanoparticles: experimental evidence of low-field deviation from the linear response theory and empirical model

Irene Andreu,^{1,2} Ainhoa Urtizberea,^{3,4} Eva Natividad^{1}*

¹ Instituto de Ciencia de Materiales de Aragón (ICMA), CSIC - Universidad de Zaragoza, Campus Río Ebro, María de Luna 3, 50018 Zaragoza, Spain

² RI Consortium of Nanoscience and Nanotechnology and Department of Chemical Engineering, University of Rhode Island, Kingston, Rhode Island, 02881, USA

³ Centro Universitario de la Defensa, Ctra. de Huesca s/n, 50090 Zaragoza, Spain

⁴ Dpto. de Física de la Materia Condensada, Universidad de Zaragoza, Pedro Cerbuna 12, 50009 Zaragoza, Spain

Address correspondence to: evanat@unizar.es.

SUPPORTING INFORMATION

Index

1. ROSENSWEIG'S MODEL OF SUPERPARAMAGNETISM AND LINEAR RESPONSE THEORY (LRT)	S3
2. MAGNETIC NANOPARTICLES AND PREPARATION OF MNPS ASSEMBLIES	S4
3. EXPERIMENTAL TECHNIQUES	S5
3.1. Transmission Electron Microscopy	S5
3.2. Magnetic measurements	S5
3.3. Determination of mass of MNPs.....	S6
3.4. Thermal measurements.....	S6
4. $M(H)$ AND ZFC/FC $M(H)$ CURVES	S7
5. ARRHENIUS PLOTS	S8
6. SOME CONSIDERATIONS ABOUT SAR VALUES	S8
6.1. SAR (H_0) and comparison with the literature.....	S8
6.2. Scaling of absolute χ'' and SAR values.....	S10
7. SPIKES IN SPH-EO.....	S10
8. $\chi''(T)$ DATA OF SAMPLE FAC-C24 AT A FIX f BUT DIFFERENT H_0	S11
9. VARIATION OF T_b WITH H_0 FOR SAMPLES FAC-E AND SPH-EO	S11
10. MODELING $\chi''(T)$ AND SAR(T) USING T_b AND SIZE DISTRIBUTION.....	S12
10.1. Theoretical basis and approximation.....	S12
10.2. Example of calculation for FAC-C24.....	S13
10.3. Modeling for SHP-E and SHP-EO	S14
11. DBF MODEL: ARRANGEMENT OF NON-IDENTICAL MNPS WITH STRONG DIPOLAR INTERACTIONS.....	S15
12. STONER-WOHLFARTH MODEL WITH APPLIED H_{dc} AND $\chi''(T)$ DATA OF SAMPLE FAC-C24 WITH DIFFERENT SUPERIMPOSED H_{dc} VALUES	S16

1. ROSENSWEIG'S MODEL OF SUPERPARAMAGNETISM AND LINEAR RESPONSE THEORY (LRT)

When an alternating magnetic field (AMF) is applied to a ferro/ferrimagnetic material, the magnetization, M , vs. applied field, H , describes a hysteresis loop due to the non-linearity and delay of M with respect to H . The area within the cycle accounts for the heat dissipated per cycle, and thus SAR can be calculated as,¹

$$SAR = \frac{f\mu_0}{\rho_{MNP}} \oint M(H)dH \quad (S1)$$

where $\mu_0 = 4\pi \times 10^{-7}$ T·m/A is the permeability of free space, ρ_{MNP} is the density of the magnetic material, and M and H are expressed in SI units (A/m).

When a magnetic nanoparticle (MNP) is subjected to an AMF whose amplitude, H_0 , is small enough as to fulfill the requirements of the linear response theory (LRT), then the value of its magnetization is directly proportional to H_0 . This means that its magnetic susceptibility, χ , depends on the AFM f , but not on H_0 . Considering χ in its complex form, $\chi = \chi' - i\chi''$, where χ' and χ'' are the in-phase and out-of-phase components of the magnetic susceptibility, respectively, and assuming a sinusoidal AMF,¹ equation S1 changes into,

$$SAR = \frac{\pi\mu_0}{\rho_{MNP}} f H_0^2 \chi'' \quad (S2)$$

which relates χ'' and the AMF parameters with the released heat power. Considering an isolated MNP, the LRT is only valid when²

$$H_0 < \frac{k_B T}{\mu_0 M_s V} \quad (S3)$$

where M_s and V are, respectively, the saturation magnetization and the (magnetic) volume of the MNP in SI units, k_B is the Boltzmann constant and T is the temperature. Equation S3 indicates that the LRT is only valid for small H_0 values, and that the maximum H_0 for LRT validity decreases with increasing V .

According to Rosensweig's model of superparamagnetism,¹ the out-of-phase ac susceptibility, indicative of dissipative processes, can be expressed as,

$$\chi'' = \chi_0 \cdot \frac{2\pi f \tau}{1+(2\pi f \tau)^2} \quad \text{with} \quad \chi_0 \cong \frac{\mu_0 M_s^2 V}{3k_B T} \quad (S4)$$

where χ_0 is the static susceptibility (isolated MNP), and τ is the magnetic moment relaxation time, which stands for the Néel relaxation time in case of an immobilized MNP. The simplified expression for this time is,

$$\tau \equiv \tau_N = \tau_0 \exp\left(\frac{E_{b0}}{k_B T}\right) \quad (S5)$$

where τ_0 is the attempt time, $\tau_0 = 10^{-8} - 10^{-10}$ s, and E_{b0} is the barrier energy for magnetization reversal, created by the anisotropy energy of the MNPs. This Arrhenius law reflects the effect of temperature in the relaxation time and, accordingly, in out-of-phase ac susceptibility and in SAR. χ'' has a maximum (χ''_{\max}) at $2\pi f \tau = 1$ (eq. S4), whose value is $\chi_0/2$. The T at which this maximum takes place is called the blocking temperature (T_b), which delimits the FM ($T < T_b$) and the SPM ($T > T_b$) behaviour and fulfills,

$$-\ln(2\pi f) = \ln(\tau_0) + \frac{E_{bo}}{k_B T_b} \quad (S6)$$

2. MAGNETIC NANOPARTICLES AND PREPARATION OF MNPS ASSEMBLIES

In this work we used the following chemicals: absolute ethanol, iron acetylacetonate (> 99.9% trace metal), benzyl ether (99%), 1,2-hexadecanediol (97%), oleic acid (90%), oleylamine (>70%), n-hexane (>99%), n-tetracosane (>99%), dichloromethane (99%), nitric acid (70%, 99.999% trace metal basis) and hydrochloric acid (37 %wt in H₂O, 99.999% trace metals basis) were purchased from Sigma Aldrich at the indicated purities and used as received; the epoxy resin Epofix™ was purchased from Electron Microscopy Sciences and used following the supplier instructions.

Faceted (FAC) magnetic nanoparticles were obtained as described previously³ adapting the original seeded growth method by Sun *et al.*^{4,5} Briefly, MNPs were synthesized by the thermal decomposition of iron acetylacetonate in benzyl ether in the presence of 1,2-hexadecanediol, oleic acid and oleylamine. Seeded growth was used to achieve FAC NPs with a size around 14 nm in 20 growth steps. The obtained nanoparticles, identified as magnetite, are coated with oleic acid and oleylamine and dispersed in n-hexane. Spherical (SPH) highly monodisperse magnetite nanoparticles were purchased from Ocean Nanotech (SOR-18). They were provided with oleic acid coating and suspended in chloroform.

For preparation of samples containing different MNPs and/or arrangements, aliquots of the FAC/SPH MNP suspensions were used. Organic solvent (n-hexane or chloroform) was first evaporated. MNP to be dispersed into epoxy resin were afterwards washed several times in dichloromethane and ethanol to remove as much as possible the surfactant not adsorbed onto the MNP surface and provide a better dispersion in epoxy. Samples FAC-E and SPH-E were obtained dispersing (stirring) FAC/SPH MNPs in epoxy resin inside a BEEM embedding capsule (5.6 mm inner diameter) in an approximate ratio of 0.1 mg of MNPs per g of sample (epoxy + MNPs). After curing at ambient temperature, an additional overnight curing at 60°C were performed to these samples to prevent any difference related to thermal history during measurements. After demolding, epoxy blocks were shaped as a short cylinder with one end finished in a truncated pyramid, with an aspect ratio close to 1. Sample FAC-C24 was prepared by dispersing FAC MNPs in melted n-tetracosane in an approximate ratio of 0.01 mg of MNPs per g of sample (MNPs + n-tetracosane). After keeping at 100°C under ultrasonication in a test tube, the liquid dispersion was then injected to a special-purpose cylindrical quartz sample holder (*c.a.* 20mm in length and 5mm in diameter, in form of a small bottle), quickly solidified in a water-ice bath and sealed with an epoxy adhesive. This sample was measured inside the container, given the low melting temperature of n-tetracosane. Sample SPH-EO were obtained dispersing (stirring) SPH MNPs in epoxy resin inside a small quartz container in form of test tube in an approximate ratio of 0.01 mg of MNPs per g of sample (epoxy + MNPs). During the curing at ambient temperature, the tube was placed at *c.a.* 5mm over a static magnetic field generated with a permanent magnet (N42 magnet S-30-07-N, Supermagnete) to promote alignment of the SPH NPs parallel to the tube axis. After curing, formed MNP spikes were visible with the naked eye (see SI). After demolding, the epoxy block was grinded and polished to fit a BEEM embedding capsule similar to those of FAC-E and SPH-E, with the spikes parallel to the cylinder axis. Finally, the sample was subjected to an additional overnight curing at 60°C. All samples have compatible shape and size both with the instrumentation used for SAR and magnetic characterization

(except FAC-C24 for magnetic measurements with the applied field perpendicular to the cylinder axis direction, which was not measured), and the same specimen was used throughout these experiments.

3. EXPERIMENTAL TECHNIQUES

3.1. Transmission Electron Microscopy

A JEOL 2000 FXII TEM (Transmission Electron Microscope) operating at an acceleration voltage of 200 kV was used to characterize the size and morphology of MNPs and MNP arrangements. On the one hand, to analyze the size and shape of MNPs, the FAC/SPH MNP suspensions were dropped on a carbon coated Cu TEM grid, and the solvent was let evaporate. From TEM micrographs, the size of 300 NPs was measured and the obtained histogram was fitted to a Gaussian distribution to determine the mean size and standard deviation. In the case of SPH NPs, the diameter was taken as the relevant measure. In case of FAC NPs, the equivalent sphere diameter was estimated. On the other hand, to determine the morphology of MNPs assemblies in each sample (SPH-E, FAC-E, FAC-C24 and SPH-EO), the samples were cut and sliced by ultramicrotomy using a diamond knife (DIATOME Ultra 35°) to obtained cross-sections (perpendicular to the cylinders axis). In addition, for sample SPH-EO, longitudinal sections (parallel to the cylinders axis) were sliced. For this purpose, the sample was embedded transversally in epoxy resin inside a flat mold. All these ultramicrotome slices were observed by TEM.

3.2. Magnetic measurements

First magnetization curves, $M(H)$, and zero-field cooled/field cooled magnetization curves, ZFC/FC $M(T)$, were acquired using an MPMS-XL SQUID magnetometer (Quantum Design). $M(H)$ was determined at 300 K using dc fields between 0 and 5 T. To determine the saturation magnetization, M_s , of the magnetic volume of FAC and SPH NPs, dia/paramagnetic contributions (of surfactant, container, dead layer, etc.) were subtracted through a linear fit of the linear dependence between 3 and 5 T. ZFC/FC $M(T)$ curves were acquired under 3 kA/m (38 Oe) between 10 and 320 K. The samples were cooled down from room temperature in absence of field (the magnet was reset at room temperature to avoid any stray fields). Once the lowest temperature was achieved, the selected static magnetic field was applied and the M was measured upon heating. After the maximum T was reached, the sample was cooled down again, this time under the action of the static field, and the M was again measured upon heating. Due to the low static field used, no dia/paramagnetic corrections were performed. The out-of-phase magnetic susceptibility, χ'' , was measured both in the MPMS-XL SQUID magnetometer and in the Physical Properties Measurement System (PPMS) with an ACMS (AC Measurement System) option (Quantum Design). $\chi''(T)$ curves at fixed H_0 and several frequencies (Figure 3A, D, G, J) were obtained with the former, while $\chi''(T)$ curves at several H_0 and f (Figure 5C and Figure S7), and also with superimposed dc applied field (Figure S11) were acquired with the later. Most measurements were performed in the range 10 and 320 K, using H_0 values ranging between 0.22 and 1.11 kA/m (2.74 to 14 Oe), and f values between 10 Hz and 10 kHz. Data was converted from the cgs system to the SI using the density of bulk magnetite, 5.18 g/cm³. The mass of MNPs was determined from M_s values as explained below.

3.3. Determination of mass of MNPs

Sample concentration (mass of magnetic material per mass of sample) was determined through a combination of elemental analysis and magnetic measurements. The first magnetization curves $M(H)$ of sacrificial samples of MNPs FAC and SPH, prepared evaporating the solvent of aliquots of the initial suspensions inside gelatine capsules, were measured. These same samples were afterwards digested in *aqua regia* at 90°C and diluted in distilled water for Inductively Coupled Plasma-Optical Emission Spectroscopy (ICP-OES, Jobin Yvon 2000) to determine the total Fe content. Assuming stoichiometric magnetite Fe_3O_4 , the M_S for FAC and SPH NPs was calculated as explained in the previous section. Using these M_S values to scale the $M(H)$ curves of all the samples, the mass of magnetic material (m_{MNP}) in each sample was obtained, and the average concentration of the samples was calculated dividing by the total sample mass.

3.4. Thermal measurements

The heating ability of the samples was determined using a unique adiabatic magnetothermal device described previously.^{6,7} With this setup, the Specific Absorption Rate (SAR, heat power dissipated per unit mass of magnetic material in presence of an alternating magnetic field) is calculated using the traditional pulse heating method of adiabatic calorimetry, with the difference that an AMF pulse is applied instead of a heat pulse. The sample is first set under vacuum and afterwards cooled down to 170 K in absence of ac-field. Then, a gentle heating ramp is established by means of the temperature control of the system. This control is also necessary to enable that the radiation shield is at the same temperature of the sample, assuring the adiabatic conditions of the experiment. SAR is measured during this heating ramp. As an example, Figure S1 (left) displays the temperature-vs.-time trend of sample FAC-E during SAR measurements. Ac-field pulses of duration Δt are applied to the sample, which undergoes self-heating. From the $T(t)$ trends during and after each ac-field pulse application, ΔT is calculated as schematized in Figure S1 (right), and assigned to the temperature $T = (T_1 + T_2)/2$. From $\Delta T(T)$ data, SAR is calculated as:

$$SAR(T) = \frac{C(T)}{m_{MNP}} \cdot \frac{\Delta T(T)}{\Delta t} \quad (S7)$$

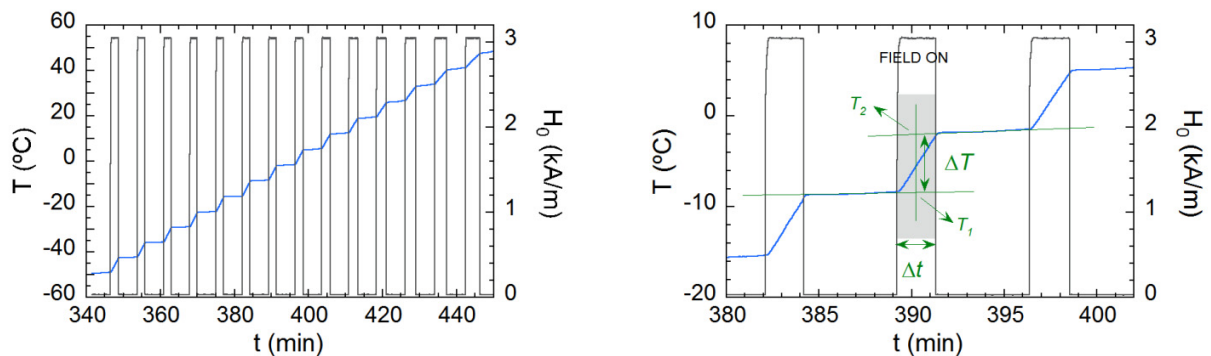


FIG S1. Left: experimental example of temperature (blue line) vs. time trend during SAR measurements using the pulse-heating method. The grey line delimits the time interval, Δt , in which the alternating magnetic field is applied. Right: example of ΔT calculation.

MNPs	Sample	Medium	m_{CONT} (g)	m_{N27} (g)	m_{med} (g)	m_{MNP_s} (mg)
SPH	SPH-E	epoxy resin	-	-	0.07368	14.08
	SPH-EO	epoxy resin	-	-	0.05091	0.39
FAC	FAC-E	epoxy resin	-	-	0.06827	6.06
	FAC-C24	n-tetracosane	0.39518	0.03406	0.10160	0.92

TABLE S1. Specimen characteristics used to calculate the heat capacity (C): dispersive medium, mass of container (m_{CONT}), mass of sealant (m_{N27}), mass of dispersive medium (m_{med}) and mass of nanoparticles (m_{MNP_s}). The latter is also used in equation S7.

where $C(T)$ is the thermal dependence of the specimen (sample + container) heat capacity and m_{MNP} is the mass of magnetic material. C is calculated as $C = \sum_i c_i \cdot m_i$, where c_i and m_i are, respectively, the specific heat capacity (J/g·K) and mass of each component of a measured specimen. Table S1 collects these values for all measured specimens. The specific heat of the epoxy resin Epofix, and those of FAC-C24 quartz container and epoxy adhesive were experimentally determined in the range 100-320 K by Differential Scanning Calorimetry (DSC) with a Q1000 device from TA Instruments, using indium and sapphire as calibrants. The specific heat of magnetite⁸ and n-tetracosane⁹ were obtained from the literature.

4. $M(H)$ AND ZFC/FC $M(H)$ CURVES

First magnetization curves, $M(H)$, were acquired with the applied dc field both parallel and perpendicular to the sample (cylinder) axis (except for sample FAC-C24 with the applied dc field perpendicular to the cylinder axis, due to size restrictions), to detect any average anisotropy of the samples (Fig. S2 left).

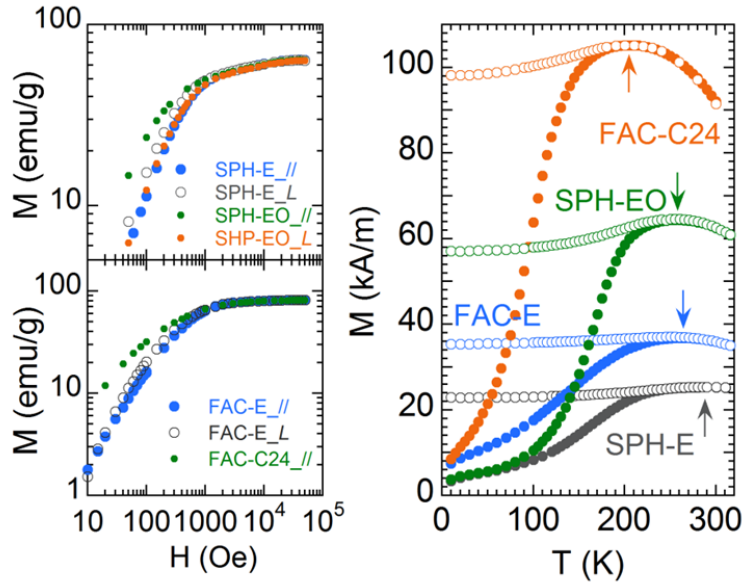


FIG S2. Left: first magnetization curves, $M(H)$, with the applied dc field parallel (//) and perpendicular (L) to the cylinder axis. Right: Zero-field cooled/field cooled magnetization curves ZFC/FC $M(T)$, with the applied dc field (3 kA/m \equiv 38 Oe) parallel to the cylinder axis.

Zero-field cooled/field cooled magnetization curves ZFC/FC $M(T)$, were measured with the applied dc field (3 kA/m \equiv 38 Oe) parallel to the cylinder axis (Fig. S2 right). All samples display ZFC/FC $M(T)$ features indicative of strong magnetic interactions.¹⁰ First, both FC $M(T)$ curves decrease and reach a plateau towards low temperatures, displaying a concave FC $M(T)$ curve at low temperatures. In absence of interactions the FC curves should increase and be convex towards low temperatures. The presence of weak magnetic interactions should decrease magnetization, but $M(T)$ should still remain convex below the maximum of the FC $M(T)$ curve. Also, in non-interacting systems, the temperature at the maximum of ZFC $M(T)$ curves (determines the onset of the superparamagnetic behavior and is related to E_b) is appreciably lower than the temperature at which the FC and ZFC $M(T)$ curves collapse, and the majority of the MNPs gets unblocked.

5. ARRHENIUS PLOTS

The T_b obtained from $\chi''(T)$ and SAR(T) data in main manuscript for samples SPH-E (Figs. 3A and B), FAC-E (Figs. 3D and E) and SPH-EO (Figs. 3J and K) are represented according to eq. S6. From the linear fit of these plots, $\ln \tau_0^*$ and E_b can be obtained (see eq. 6 in main manuscript).

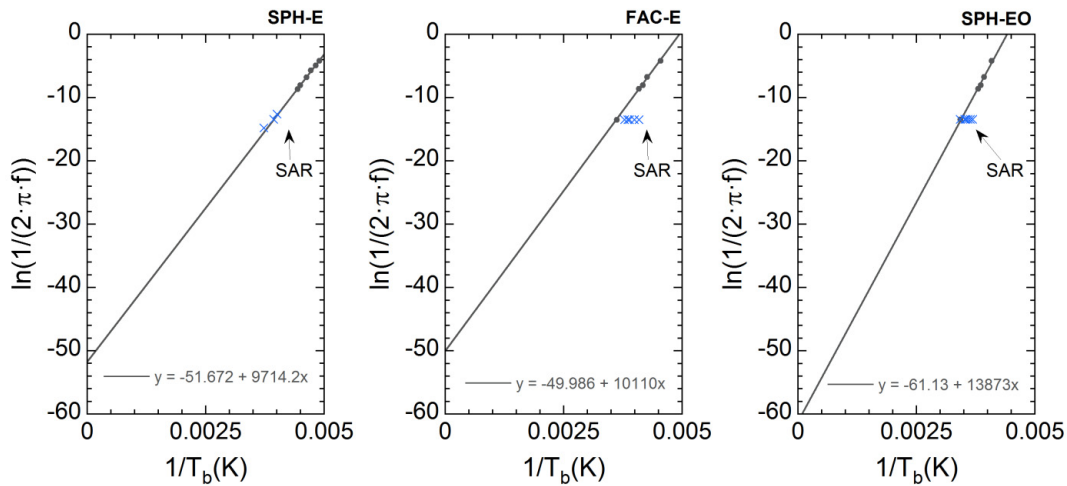


FIG S3. Arrhenius plots of FAC-E, SPH-E and SHP-EO. Linear fits were done considering only black circles, *i.e.*, $\chi''(T)$ data obtained at the same H_0 and SAR data (111 kHz) extrapolated to this H_0 (see Fig. S8). T_b values obtained from original SAR(T) data appear as blue crosses.

6. SOME CONSIDERATIONS ABOUT SAR VALUES

6.1. SAR (H_0) and comparison with the literature

Focusing now on SAR values, it is evident that oriented arrangements (FAC-C24, SPH-EO) present much higher SAR values than randomly oriented arrangements (SAR of FAC-C24 is 19 times higher than that of FAC-E, SAR of SPH-EO is 5 times higher than that of SPH-E). The randomly oriented arrangements (FAC-E, SPH-E) present very similar values. According to the LRT, SPH MNPs, with the narrowest size distribution, should have the sharpest $\chi''(T)$ and SAR(T) curves. However, the sharpest trends are found in FAC-C24 at low H_0 . The high E_{arr} in FAC-C24 value sharpens these curves, erasing the widening effect of the size distribution, and allowing high SAR values. Fig. S4 displays the variation of the energy dissipated per

AMF cycle (SAR/f) in function of H_0 for samples FAC-E and FAC-C24. In FAC-E and also in FAC-C24 at T_b (SAR_{max}), data follow a power law αH_0^m with $m = 1.9$, typical of SPM MNPs. However, if m is evaluated in FAC-24 at a fix T , a gradual m variation is found, from 3 at 200 K to 1.4 at 300 K. This is a direct consequence of the $T_b(H_0)$ dependency. Accordingly, if the MNPs were a few nanometers larger such as $T_b(H=0)$ is slightly over room temperature, T_b and thus SAR_{max} could be adjusted to room temperature by increasing H_0 . It is also possible that a specimen of FAC MNPs with arrangements showing an overall preferential orientation within the sample could have resulted in SAR values even higher than those of FAC-C24.

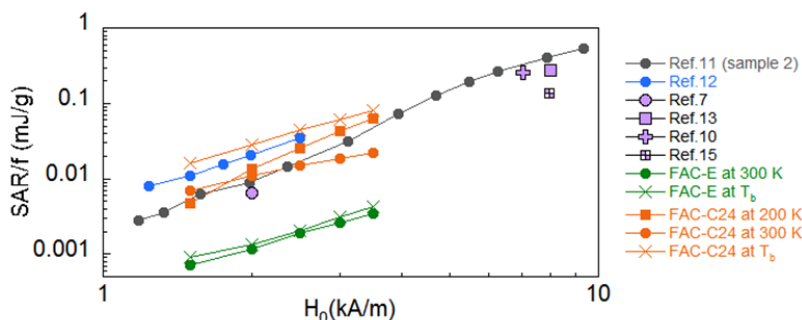


FIG S4. Comparison of SAR/f values in this work with high SAR values reported in the literature. SAR values of this work are orange (FAC-E) and green (FAC-C24), and are depicted at T_b (SAR_{max}, crosses), at 300 K (circles) and at 200 K (squares).

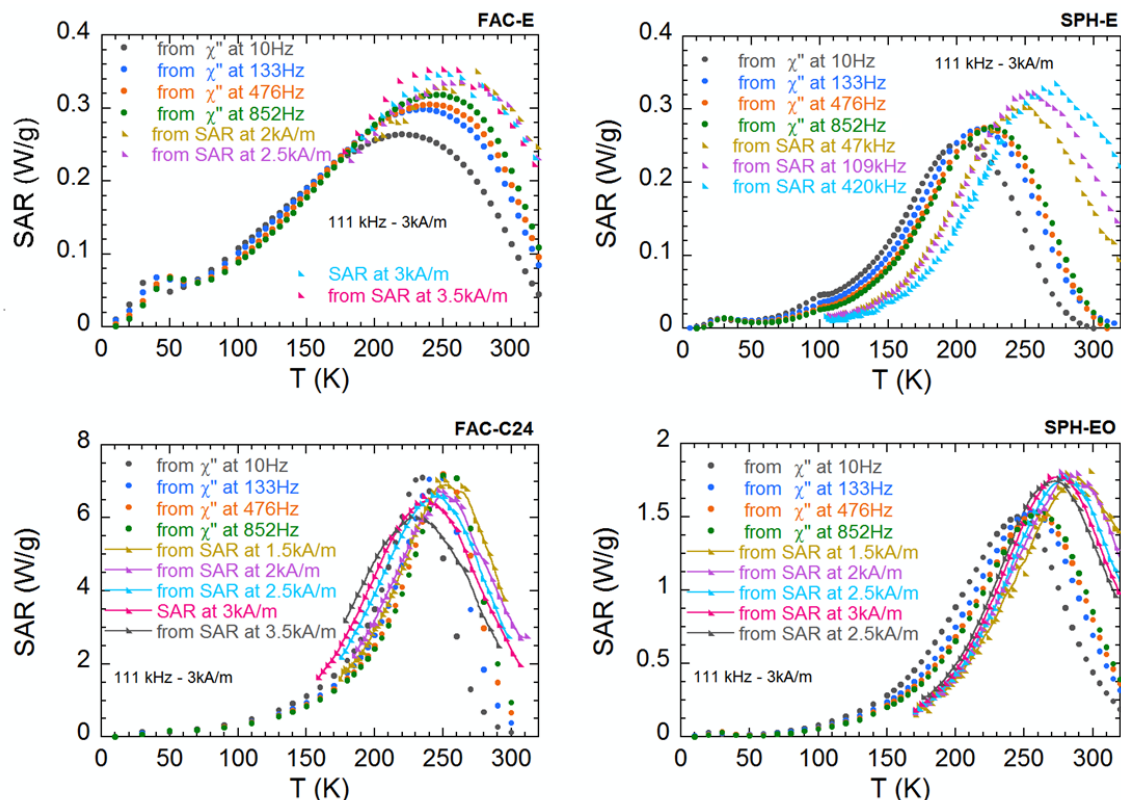


FIG S5. Scaling of $\chi''(T)$ and SAR(T) absolute values (data in Figs. 3A, B, D, E, G, H, J and K in main manuscript) into SAR at 111 kHz and 3kA/m. SAR directly measured with these field parameters is shown as-recorded.

The SAR/f values of FAC-C24 were comparable (Fig. S4) with high SAR values reported in the literature, obtained with H_0 ranging between 1 and 10 kA/m. Note that part of this range may be out of the limits of the LRT validity for some samples. These samples are iron oxide MNPs including: i) bacterial magnetosomes^{11,12} of *c.a.* 34 nm forming oriented chains; ii) the FluidMAG-UC/A from Chemicell GmbH⁷, which contains 50 nm-clusters of MNPs of *c.a.* 15 nm; iii) nanocubes with 19 nm in average diameter¹³; nanoflowers (39 nm) of densely packed nanocrystals with sizes ranging between *c.a.* 5–15 nm¹⁴; and iv) nanocrystals of 2–5 nm forming 20–40 nm aggregates¹⁵. These data highlight the essential role of the MNP arrangement on SAR and the high potential of controlling MNP assembly to increase SAR values.

6.2. Scaling of absolute χ'' and SAR values

Measured $\chi''(T)$ and SAR(T) absolute values (data in Figs. 4A, B, D, E, G, H, J and K in main manuscript) have been turned into SAR at 111 kHz and 3kA/m using eq. S2 but neglecting the scaling in temperature. That is, $\chi''(T)$ data have been transformed by directly multiplying by $\frac{\pi\mu_0}{\rho_{MNP}} fH_0^2$, and SAR(T) data by dividing by the experimental fH_0^2 product and multiplying by the nominal (111 kHz and 3kA/m) product. In all cases (Fig. S5), slight differences in SAR_{max} are found, although SAR data obtained from both types of measurements show good continuity, hinting at the soundness of this expression.

7. SPIKES IN SPH-EO

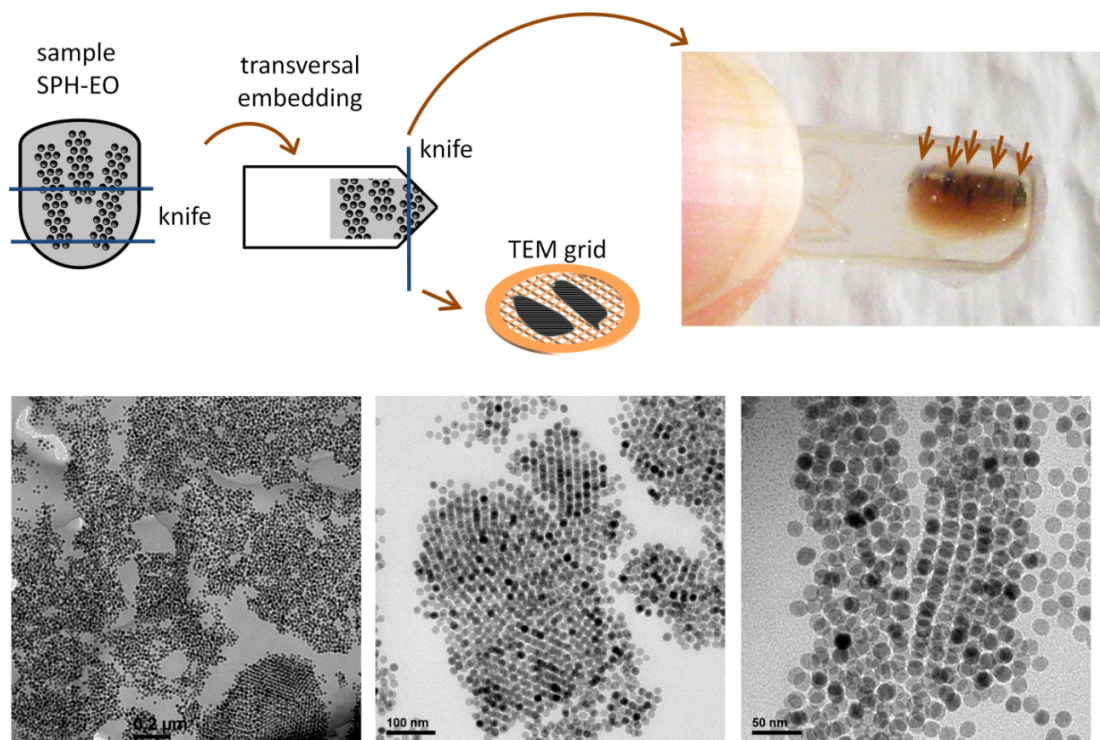


FIG S6. Top-left: scheme illustrating sample preparation for longitudinal (parallel to the cylinders axis) sectioning of SPH-EO for ultramicrotomy and TEM observation. Top-right: picture of part of sample SPH-EO embedded transversally in epoxy resin (inside a flat mold) in which MNP spikes can be observed (arrows). Bottom: TEM images of longitudinal sections.

Sample SPH-EO was prepared embedding SPH MNPs into epoxy resin, in presence of a strong static magnetic field parallel to the cylindrical mold. As a result, it presents a macroscopic MNP arrangement

in form of spikes oriented parallel to the tube axis and visible to the naked eye (Fig. S6). TEM images revealed that the cross-section of the macroscopic spike structure is formed by highly-packed ordered areas surrounded by more disperse and disordered zones (Figure 2L-N in main manuscript), TEM images of sections parallel to the sample axis were also acquired, revealing similar arrangements (Fig. S6).

8. $\chi''(T)$ DATA OF SAMPLE FAC-C24 AT A FIX f BUT DIFFERENT H_0

Additional $\chi''(T)$ data sets to that of Fig. 3 in the main manuscript, each at fix f but different H_0 , have been recorded for sample FAC-C24 using a PPMS instrument. These data (Fig. S7) show that the effect observed with H_0 in SAR(T) measurements is present at values as low as 0.16 kA/m (2 Oe), well within the LRT limit for these MNPs.

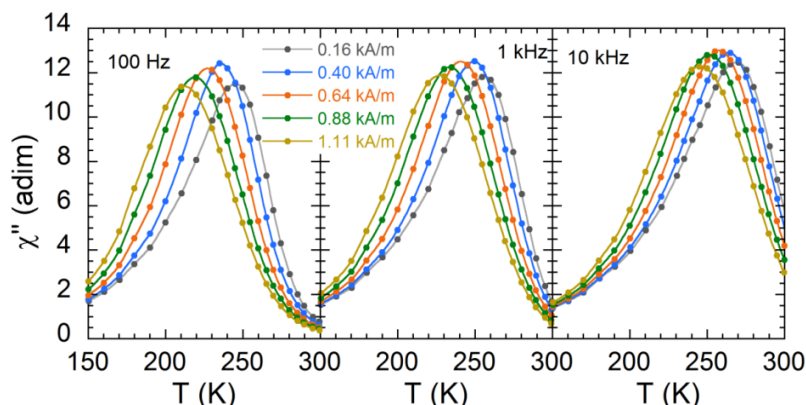


FIG S7. $\chi''(T)$ data recorded under an ac field frequency of 100 Hz (left), 1kHz (middle) and 10 kHz (right) and amplitudes 0.16 – 1.11 kA/m.

9. VARIATION OF T_b WITH H_0 FOR SAMPLES FAC-E AND SPH-EO

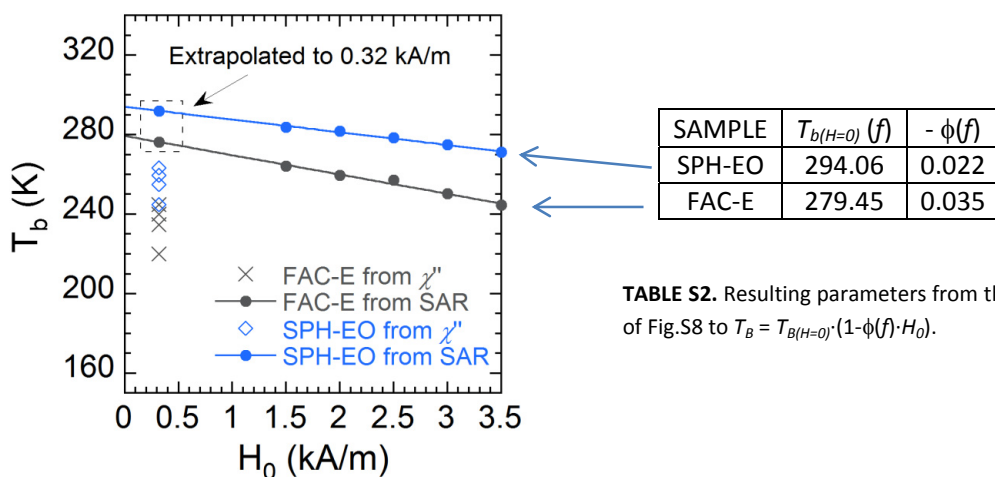


TABLE S2. Resulting parameters from the linear fits of Fig.S8 to $T_B = T_{B(H=0)}(1-\phi(f)\cdot H_0)$.

FIG S8. T_b data vs. H_0 for FAC-E (black) and SPH-EO (blue). SAR data (circles) were recorded at 111 kHz (FAC-E) and 112 kHz (SPH-EO). χ'' data (crosses) were recorded at 10, 133, 476 and 852 Hz. The points extrapolated to 0.32 kA/m are used in Fig. S3.

Similarly to FAC-C24, samples FAC-E and SPH-EO display a linear T_b dependence on H_0 at low ac fields (Fig. S8) that can be described as $T_b = T_{b(H=0)} \cdot (1 - \phi(f) \cdot H_0)$, where $T_{b(H=0)}$ is the T_b value at zero H_0 ($T_{b(H=0)}$ depends on f), and $-T_{b(H=0)} \cdot \phi(f)$ is the slope (eq. 4 in main manuscript).

10. MODELING $\chi''(T)$ AND SAR(T) USING T_b AND SIZE DISTRIBUTION

10.1. Theoretical basis and approximation

The magnetic moment of a system consisting of an arrangement of MNPs is the cumulative sum of the magnetic moment of every MNPs contribution. Accordingly, the out-of-phase ac susceptibility, χ'' , calculated as the ratio between the total magnetic moment per unit volume (total volume) and the applied field amplitude, H_0 , can be expressed as,

$$\chi'' = \sum_{j=1}^N \chi_j'' \quad (S8)$$

where χ_j'' is the magnetic moment of a MNP of volume V_j , divided by the total volume and H_0 , and N the number of MNPs.

If we use a histogram to account for the different sizes of MNPs, we can discretize the V_j values present in the system and approximate eq. S8 as,

$$\chi'' \cong \sum_{i=1}^{N_V} \chi_i'' \cdot f_i \quad \text{with} \quad f_i = \frac{N_{Vi} V_i}{\sum_{i=1}^{N_V} N_{Vi} V_i} \quad (S9)$$

Where N_V is the number of different volumes considered (histogram bins), N_{Vi} is the number of MNPs of volume V_i (histogram counts of each bin), χ_i'' is the out-of-phase ac susceptibility of every MNP of volume V_i ($\chi_i'' \equiv \chi_j''$) and f_i is the volume fraction occupied by all the MNPs of volume V_i .

According to Rosensweig's model of superparamagnetism, for each particle from population i ,

$$\chi_i'' = \chi_{0i} \cdot \frac{2\pi f \tau_i}{1 + (2\pi f \tau_i)^2} \quad \text{with} \quad \chi_{0i} = \frac{\mu_0 M_S V_i}{3k_B T} \quad (S10)$$

And according to eq. S5,

$$\tau_i \equiv \tau_{Ni} = \tau_0 \exp\left(\frac{E_{bi}}{k_B T}\right) \quad (S11)$$

where τ_0 is the attempt time, E_{bi} is the barrier energy for magnetization reversal of the MNPs of volume V_i and k_B is the Boltzmann constant. In order to simplify the calculation of χ'' , we can assume that χ_i'' presents a sharp maximum (of value $\frac{\chi_{0i}}{2}$) at $2\pi f \tau_i = 1$, i.e., at the blocking temperature T_{bi} , and substitute this function by a Delta function,

$$\chi_i'' \cong \frac{\chi_{0i}}{2} \cdot \delta(T - T_{bi}) \quad \text{with} \quad T_{bi} = \frac{E_{bi}}{-k_B \ln(2\pi f \tau_0)} \quad (S12)$$

Then,

$$\chi'' \cong \sum_{i=1}^{N_V} \frac{\chi_{0i}}{2} \cdot \delta(T - T_{bi}) \cdot f_i \quad (S13)$$

Note that this new function $\chi''(T)$ is identical to the graphical representation of $f_i \cdot \frac{\chi_{oi}}{2}$ vs. T_{bi} for the N_V points. Also, we define E_{bi} as,

$$E_{bi} = E_{arr} + K_{app} \cdot V_i \quad (S14)$$

where K_{app} is an apparent magnetic anisotropy constant, which we assume independent of V_i , and E_{arr} is the barrier energy assigned to the MNP arrangement. This is the basis used to model $\chi''(T)$ and SAR(T).

10.2. Example of calculation for FAC-C24

Starting from the normal fit to the experimental size distribution of FAC MNPs obtained from TEM analysis (see main manuscript, Fig. 1) we set $N_V = 30$ (one histogram bin each 0.5 nm in diameter). From this data, we calculate V_i , N_{Vi} and f_i according to the previous section (see Table S3).

i	Size (nm)	V_i (m ³)	N_{Vi}	$V_i \cdot N_{Vi}$ (m ³)	f_i	$K_{app} \cdot V_i / k_B$ (K)	E_{arr} / k_B (K)	E_{bi} / k_B (K)	T_{Bi} (K)	$f_i \cdot \chi_{oi} / 2$ (adim)
1	7	1.80E-25	0.65	1.17E-25	0.0001	171	6050	6221	184.00	0.000
2	7.5	2.21E-25	1.28	2.82E-25	0.0002	211	6050	6261	185.16	0.001
3	8	2.68E-25	2.38	6.39E-25	0.0005	256	6050	6306	186.49	0.002
4	8.5	3.22E-25	4.23	1.36E-24	0.0010	306	6050	6356	188.00	0.005
5	9	3.82E-25	7.15	2.73E-24	0.0020	364	6050	6414	189.69	0.011
6	9.5	4.49E-25	11.46	5.14E-24	0.0038	428	6050	6478	191.59	0.024
7	10	5.24E-25	17.46	9.14E-24	0.0067	499	6050	6549	193.69	0.049
8	10.5	6.06E-25	25.29	1.53E-23	0.0113	578	6050	6628	196.02	0.094
9	11	6.97E-25	34.81	2.43E-23	0.0178	664	6050	6714	198.58	0.168
10	11.5	7.96E-25	45.53	3.63E-23	0.0266	759	6050	6809	201.38	0.283
11	12	9.05E-25	56.59	5.12E-23	0.0376	862	6050	6912	204.44	0.447
12	12.5	1.02E-24	66.85	6.84E-23	0.0502	975	6050	7025	207.76	0.664
13	13	1.15E-24	75.05	8.63E-23	0.0634	1096	6050	7146	211.36	0.927
14	13.5	1.29E-24	80.06	1.03E-22	0.0758	1228	6050	7278	215.25	1.218
15	14	1.44E-24	81.17	1.17E-22	0.0857	1369	6050	7419	219.44	1.507
16	14.5	1.60E-24	78.21	1.25E-22	0.0917	1521	6050	7571	223.93	1.756
17	15	1.77E-24	71.61	1.27E-22	0.0930	1684	6050	7734	228.75	1.929
18	15.5	1.95E-24	62.31	1.21E-22	0.0893	1858	6050	7909	233.90	1.998
19	16	2.14E-24	51.53	1.11E-22	0.0812	2044	6050	8094	239.39	1.953
20	16.5	2.35E-24	40.49	9.52E-23	0.0700	2242	6050	8292	245.24	1.802
21	17	2.57E-24	30.24	7.78E-23	0.0572	2452	6050	8502	251.45	1.570
22	17.5	2.81E-24	21.46	6.02E-23	0.0443	2675	6050	8725	258.04	1.292
23	18	3.05E-24	14.48	4.42E-23	0.0325	2911	6050	8961	265.02	1.005
24	18.5	3.32E-24	9.28	3.08E-23	0.0226	3160	6050	9210	272.39	0.739
25	19	3.59E-24	5.65	2.03E-23	0.0149	3423	6050	9473	280.18	0.513
26	19.5	3.88E-24	3.27	1.27E-23	0.0093	3701	6050	9751	288.38	0.337
27	20	4.19E-24	1.80	7.54E-24	0.0055	3993	6050	10043	297.02	0.210
28	20.5	4.51E-24	0.94	4.25E-24	0.0031	4300	6050	10350	306.10	0.123
29	21	4.85E-24	0.47	2.27E-24	0.0017	4622	6050	10672	315.63	0.069
30	21.5	5.20E-24	0.22	1.15E-24	0.0008	4960	6050	11010	325.63	0.036

TABLE S3. Data from the modeling of the $\chi''(T)$ of FAC-C24 measured at 11 Oe (0.88 kA/m) and 1 kHz.

In this example we aim to reproduce the $\chi''(T)$ data of sample FAC-C24 measured at 0.88 kA/m (11 Oe) and 1 kHz. For this purpose, we use the data obtained with the empirical model for the T_b dependence on H_0 and f (see main manuscript, eqs. 6 to 10). According to the model, both τ_0^* and E_b are independent from f but depend on H_0 . For 0.88 kA/m, $\tau_0^* = 3.29 \cdot 10^{-19}$ s and $E_b / k_B = 7909$ K, as obtained from the Arrhenius plot of the $\chi''(T)$ maxima. Accordingly, this E_b value is considered as the E_{bi} assigned to the V_i

corresponding to the maximum of $f_i \chi_{0i}/2$ ($E_{b,max}$ and V_{max} , respectively, in this case for $i = 18$, line in bold in table S3).

Using these $E_{b,max}$ and V_{max} values and eq. S14 (with $E_{bi} = E_{b,max}$ and $V_i = V_{max}$), K_{app} (and consequently also E_{arr}) is adjusted until the calculated $f_i \chi_{0i}/2$ vs. T_{bi} plot reproduces the experimental $\chi''(T)$ at temperatures near and above T_b (see Fig. S9, left). $f_i \chi_{0i}/2$ is scaled in absolute value if necessary. For this example, $K_{app} = 13.15 \text{ kJ/m}^3$ and $E_{arr}/k_B = 6050 \text{ K}$. Fig. S9 (right) shows the result of the approximation made at using the Delta function (eq. S13) to simplify the calculation of χ'' . It can be observed that the approximation (dashed line) is just a bit shifted in temperature with respect to the total sum (dotted line).

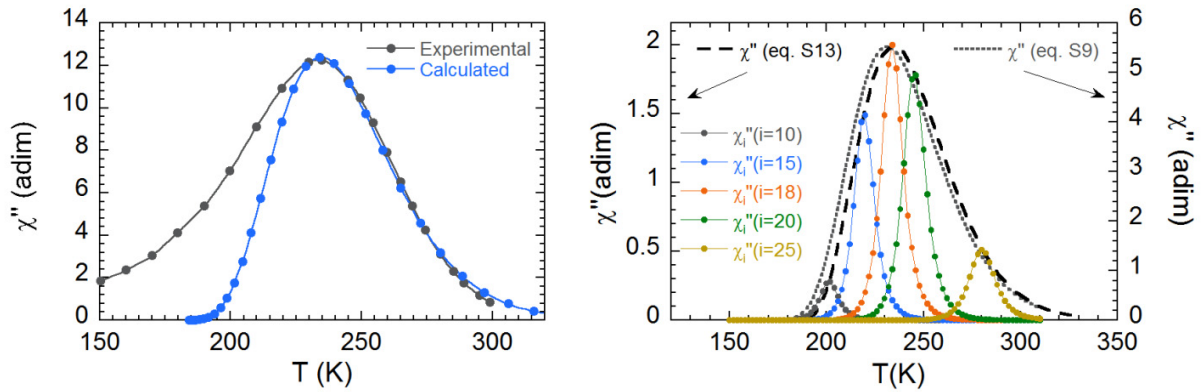


FIG S9. Modeling of the $\chi''(T)$ of FAC-C24 measured at 11 Oe (0.88 kA/m) and 1 kHz. Left: scaled $f_i \chi_{0i}/2$ vs. T_{bi} (calculated) reproducing $\chi''(T)$ (experimental) at temperatures near and above T_b . Right: $\chi_i''(T)$ according to eq. S9 for several i values (circles); $\chi''(T)$ according to eq. S8 (dotted line) and $\chi''(T)$ according to eq. S12 (dashed line), calculated as $f_i \chi_{0i}/2$ vs. T_{bi} .

10.3. Modeling for SHP-E and SHP-EO

In the case of SPH-E, given that all $\chi''(T)$ and SAR(T) data show a good collapse (Fig. 3C in main manuscript), the parameters resulting from the modeling are common for all curves. These are $K_{app} = 56.99 \text{ kJ/m}^3$ and $E_{arr}/k_B = 0 \text{ K}$ (Fig. S10 left). The case of sample SHP-EO is more similar to that of FAC-C24. Modeling of $\chi''(T)$ data derived $E_{arr}/k_B = 3676 \text{ K}$ and $K_{app} = 59.83 \text{ kJ/m}^3$.

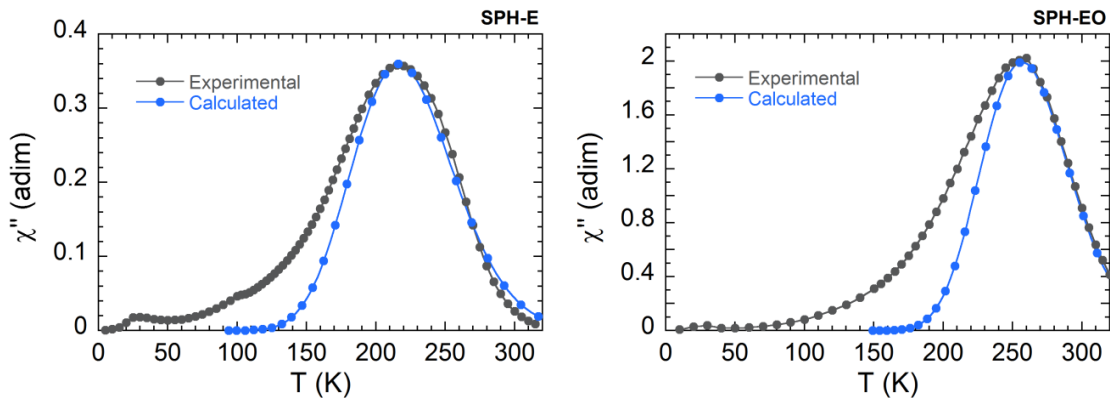


FIG S10. Modelling of the $\chi''(T)$ of SPE-E (left) and SPH-EO (right) measured at 0.32 kA/m (4 Oe) and 133 Hz as explained in previous sections.

11. DBF MODEL: ARRANGEMENT OF NON-IDENTICAL MNPS WITH STRONG DIPOLAR INTERACTIONS

The Dormann-Bessais-Fiorani¹⁶ (DBF) model assumes that relaxation time can be deduced from the Neel-Brown model through the Kramers escape rate theory, but with an energy barrier E_b modified by the dipolar energy. The model calculates the interaction energy in the case of an assembly of non-identical MNPs as,

$$E_{bint} = \frac{\mu_0}{4\pi} M_S^2 \bar{V} \sum_i b_i L \left(\frac{\mu_0}{4\pi} \frac{M_S^2 \bar{V} a_i}{k_B T} \right) \quad \text{with} \quad a_i = \frac{\bar{V}}{d_i^3} (3 \cdot \cos^2 \alpha_i - 1) \quad (\text{S15})$$

in SI units (note that in the original paper¹⁶ Gaussian units are used and thus the $\mu_0/4\pi$ factors are absent). In these expressions, \bar{V} is the mean particle volume, α_i is a mean angular parameter related to the MNP arrangement, d_i is the distance between the centre of two MNPs, b_i is a parameter similar to a_i that accounts for slight differences between MNPs (V and d_i) and L denotes the Langevin function. Given that the MNPs can be classified as first, second,... neighbours, we can rewrite,

$$E_{bint} \cong \frac{\mu_0}{4\pi} M_S^2 \bar{V} \left[n_1 b_1 L \left(\frac{\mu_0}{4\pi} \frac{M_S^2 \bar{V} a_1}{k_B T} \right) + n_2 b_2 L \left(\frac{\mu_0}{4\pi} \frac{M_S^2 \bar{V} a_2}{k_B T} \right) + \dots \right] \quad (\text{S16})$$

where $n_i = n_1, n_2, \dots$ are the number of first, second,... neighbours in the arrangement. Considering only first neighbours,

$$E_{bint} \cong \frac{\mu_0}{4\pi} M_S^2 V \left[n_1 b_1 L \left(\frac{\mu_0}{4\pi} \frac{M_S^2 \bar{V} a_1}{k_B T} \right) \right] \quad (\text{S17})$$

The parameter $x = \left(\frac{\mu_0}{4\pi} \frac{M_S^2 \bar{V} a_1}{k_B T} \right)$ reflects the strength of interactions through a_1 . For small x values (weak interactions) the Langevin function can mathematically be approximated as $L(x) \cong x/3$. But for $x \geq 2$ (strong interactions) the Langevin function can be approximated as $L(x) \cong 1-1/x$, and eq. S17 becomes,

$$E_{bint} \cong \frac{\mu_0}{4\pi} M_S^2 \bar{V} \cdot n_1 b_1 \left(1 - \frac{4\pi}{\mu_0} \frac{k_B T}{M_S^2 \bar{V} a_1} \right) \quad (\text{S18})$$

Since $E_b = K_{eff} V + E_{bint}$, and $\tau_N = \tau_0 \cdot \exp(E_b/k_B T)$,

$$\tau_N \cong \tau_0 \cdot e^{-n_1 b_1 / a_1} \cdot e^{(K_{eff} V + n_1 b_1 \frac{\mu_0}{4\pi} M_S^2 \bar{V}) / k_B T} \quad (\text{S19})$$

expression that stands for an Arrhenius law with a modified attempt time and a modified E_b . This formula can be rearranged as,

$$\tau_N \cong \tau_0 \cdot e^{-E_d / E_{di}} \cdot e^{(K_{eff} V + E_d) / k_B T} \quad (\text{S20})$$

where,

$$E_d = \frac{\mu_0}{4\pi} \cdot M_S^2 \bar{V} n_1 b_1 \quad \text{and} \quad E_{di} = \frac{\mu_0}{4\pi} \cdot M_S^2 \bar{V} a_1 \quad (\text{S21})$$

12. STONER-WOHLFARTH MODEL WITH APPLIED H_{dc} AND $\chi''(T)$ DATA OF SAMPLE FAC-C24 WITH DIFFERENT SUPERIMPOSED H_{dc} VALUES

The Stoner-Wohlfarth model provides an expression very similar to that of E_b in eq. 5 of the main manuscript. Note, however, that this model does not comprise thermally-induced relaxations. According to this model, the effect of a static magnetic field (H_{dc}) on the E_b that separates the two energy minima of a free single domain MNP can be expressed as ¹⁷

$$E_b(H) = E_{b0} \cdot \left(1 - \frac{H_{dc}}{H_{sw}^0}\right)^\kappa \quad (S22)$$

where H_{sw}^0 is the minimum H_{dc} value at which E_b disappears, and κ is an empirical exponent that depends on the angle formed by H_{dc} and the MNP anisotropy axis. For uniaxial anisotropy, $H_{sw}^0 = H_K / \varphi$, where $H_K = 2 \cdot K_{eff} / (\mu_0 \cdot M_S)$ is the anisotropy field (in SI units), and φ is a dimensionless parameter that depends as well on the angle formed by H_{dc} and the MNP anisotropy axis, $1 < \varphi < 2$.

Using the K_{app} value obtained for FAC-C24 and the M_S of FAC MNPs, we can estimate that $26 < H_{sw}^0 < 53$ kA/m. Comparing eq. 5 (main manuscript) and eq. S22, one can realize that in both expressions E_b coincide if $\kappa=1$, $H_{sw}^0 = 1/\varphi$ and H is replaced by H_0 . Note, however, that the apparent H_{sw}^0 value derived from eq. 5 ranges between $6 < H_{sw}^0 < 20$ kA/m for the studied frequencies, being lower than that predicted above. This suggests that a smaller field is necessary to induce similar changes in E_b . Obviously, H_{dc} (static field) cannot be directly replaced by H_0 (ac field amplitude). In order to know whether a dc field could act similarly to the AMF, $\chi''(T)$ measurements at a fix f and H_0 but with different superimposed dc fields (H_{dc}) were performed on sample FAC-C24 (Fig. S11). A similar shift in T_b was found, this time accompanied by a reduction of the χ''_{max} as H_{dc} increased. The fit of $T_b(H_{dc})$ yields a slope of 0.150 - 0.154 m/kA, in the range on those obtained for $T_b(H_0)$ at low f (see Fig. 4C in main manuscript). In conclusion, in this MNP arrangement the effect of H_{dc} and H_0 on E_b is similar, justifying the correlation between eq. 5 and eq. S22.

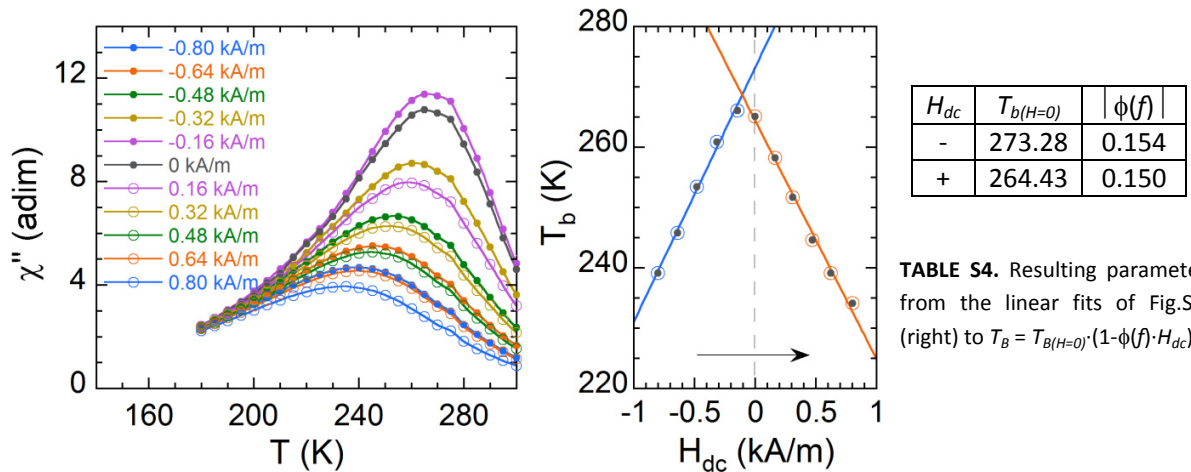


FIG S11. Left: $\chi''(T)$ data for sample FAC-C24 at 10 kHz, $H_0 = 0.22$ kA/m and several superimposed H_{dc} (parallel to the sample axis), recorded from the lowest (-0.8 kA/m) to the highest (0.8 kA/m) H_{dc} value. Right: T_b data vs. H_{dc} (black dots); blue (-) and orange (+) circles highlight data separation for the linear fit; the arrow indicates the order of the measurements.

REFERENCES

- ¹ R.E. Rosensweig, *J. Magn. Magn. Mater.*, **252** (2002) 370-374.
- ² J. Carrey, B. Mehdaoui and M. Respaud, *J. Appl. Phys.*, **109** (2011) 083921.
- ³ I. Andreu, E. Natividad, L. Solozábal and O. Roubeau, *O. J. Magn. Magn. Mater.*, **380** (2015) 341-346.
- ⁴ S. Sun and H. Zeng, *J. Am. Chem. Soc.* **124** (2002) 8204-8205.
- ⁵ S. Sun, H. Zeng, D.B. Robinson, S. Raoux, P.M. Rice, S.X. Wang and G. Li, *J. Am. Chem. Soc.* **126** (2003) 273-279.
- ⁶ E. Natividad, M. Castro and A. Mediano, *Appl. Phys. Lett.*, **98** (2011) 243119.
- ⁷ E. Natividad, M. Castro and A. Mediano, *Appl. Phys. Lett.*, **92** (2008) 093116.
- ⁸ E.F. Westrum Jr, and F. Grønvold, *J. Chem. Thermodyn.* **1** (1969) 543-557.
- ⁹ G.S. Parks, G.E. Moore, M.L. Renquist, B.F. Naylor, L.A. McClaine, P.S. Fujii and J.A. Hatton, *J. Am. Chem. Soc.* **71**, (1949) 3386-3389.
- ¹⁰ J. L. Dormann, D. Fiorani and E. Tronc, in *Advances in Chemical Physics*, ed. I. Prigogine and S. A. Rice, John Wiley & Sons, Hoboken, NJ, USA, 2007, vol. **98**, pp. 283-494.
- ¹¹ R. Hergt, R. Hiergeist, M. Zeisberger, D. Schüler, U. Heyen, I. Hilger and W.A. Kaiser, *J. Magn. Magn. Mater.*, **293** (2005) 80-86.
- ¹² A. Józefczak, T. Hornowski, A. Skumiel, M. Łabowski, M. Timko, P. Kopčanský, M. Koneracká, A. Szlaferek and W. Kowalski, *J. Magn. Magn. Mater.*, **321** (2009) 1505-1508.
- ¹³ P. Guardia, R. Di Corato, L. Lartigue, C. Wilhelm, A. Espinosa, M. Garcia-Hernandez, F. Gazeau, L. Manna and T. Pellegrino, *ACS Nano*, **6** (2012) 3080-3091.
- ¹⁴ Ph. Bender, J. Fock, Cathrine Frandsen *et al.*, *J. Phys. Chem. C*, **122** (2018) 3068-3077.
- ¹⁵ K. Kekalo, I. Baker, R. Meyers, and J. Shyong, *Nano Life*, **5** (2015) 1550002.
- ¹⁶ J L Dormann, L. Bessais and D. Fiorani, *J. Phys. C: Solid State Phys.*, **21** (1988) 2015-2034.
- ¹⁷ X. Batlle and A. Labarta, *J. Phys. D: Appl. Phys.*, **35** (2002) R15-R42.